The effect of crystal defects on 3D high resolution diffraction peaks: a FFT-based method

Komlavi Eloh, Alain Jacques, Gabor Ribarik, Stéphane Berbenni

materials

MDPI

Article

The effect of crystal defects on 3D high resolution diffraction peaks: a FFT-based method

K. Eloh[1,2,3], A. Jacques[1,3,*], G. Ribarik[3,4], S. Berbenni[2,3]

[1] Université de Lorraine, CNRS, IJL, F-54000 Nancy, France ; komlavi-senyo.eloh@univ-lorraine.fr
[2] Université de Lorraine, CNRS, Arts et Métiers Paris Tech, LEM3, F-57000 Metz, France; stephane.berbenni@univ-lorraine.fr
[3] Laboratory of Excellence on Design of Alloy Metals for low-mAss Structures (DAMAS), Université de Lorraine, France.
[4] Department of Materials Physics, Eötvös University, Budapest, Hungary.
* Correspondence: alain.jacques@univ-lorraine.fr ; Tel.: +03 72 74 26 79
Received: date; Accepted: date; Published: date

Abstract: Forward modeling of diffraction peaks is a potential way to compare the results of theoretical mechanical simulations and experimental X-Ray Diffraction data recorded during in situ experiments. As the input data are the strain or displacement field within a representative volume of the material containing dislocations, a computer-aided efficient and accurate method to generate these fields is necessary. With this aim, a current and promising numerical method is based on the use of the Fast Fourier Transform (FFT) method. However, classic FFT-based methods present some numerical artifacts due to the Gibbs phenomenon or ''aliasing'' and to ''voxelization'' effects. Here, we propose several improvements: first, a consistent discrete Green operator to remove ''aliasing'' effects and second, a method to minimize the voxelization artifacts generated by dislocation loops inclined with respect to the computational grid. Then we then show the effect of these improvements on theoretical diffraction peaks.

Keywords: Dislocations; diffraction**;** FFT-based method; Discrete Green operator; voxelization artifacts; sub-voxel method; simulated diffraction peaks; scattered Intensity

1. Introduction

X-Ray diffraction is one of the most powerful non-destructive tools to investigate materials, as their wavelength is commensurate with the distance between atoms within a crystal [1–9]. Successive improvements of both the X-Ray sources (from X-Ray tubes to third generation synchrotrons) and detectors (from photographic plates and gas counters to fast two-dimensional arrays) have led to a tremendous increase in the quantity of data recorded per unit time, allowing real time *in situ* or *in operando* measurements [10,11]. It is now possible to determine the 3D grain microstructure of a bulk material with a submicron resolution (using Topo-Tomography), to follow the evolution of the elastic strain state of the grains of a polycrystal during mechanical tests (3D-XRD, far field diffractometry), or to measure the distribution of strains within a few grains in real time (2D diffractometry) [12,13].Such experiments result in terabytes of data recorded within a few days, which need to be efficiently analyzed. In fact, only a low fraction of those data is actually treated because scientists lack both time and software for further analysis [14].

The classical techniques used to analyze the 1D or 2D diffraction patterns recorded during tests performed on polycrystalline specimens such as the Rietveld method, the square sines method to measure internal stresses, or CMWP fitting for dislocations content often rely on simplified and mathematically tractable models of a microstructure. Calculations which may involve simplifying hypothesis lead to a general formula which can be used to fit one or several parameters of the

microstructure (dislocation densities and type, internal stress tensor…) to the diffraction pattern (peak profiles, variation of the 2θ_B angle with orientation…)

During the last ten years, several authors proposed the opposite approach: forward modeling [15–22]. This requires the design of a microstructure and the simulation of its behavior (often under process or thermo-mechanical solicitation), the computation of the elastic strain field or the displacement field. The last step is the generation through a 'virtual diffractometer' of a theoretical diffraction pattern (different **G** vectors and different orientations of the lattice planes), which can be compared with the experimental one. Depending on the size of the simulated representative volume of matter and the experimental conditions such as the X-Ray beam coherence, different assumptions can be done such as a coherent beam (where the amplitudes scattered by different points add) or an incoherent beam (scattered intensities add), or for a partially coherent beam where a full calculation may be necessary. Such modeling can be quite successful and can be used to validate the different steps involved, mainly the microstructure and the constitutive law used to simulate the material's behavior.

However, as diffraction peaks contain information on different scales of a specimen: from average quantities such as Type I (average) stresses related to the peaks' positions, Type II (at grain level) stresses related to its width, and Type III stresses (near the core of defects such as dislocations) related to the peaks' tails, a realistic simulation of a diffraction peak requires a description of a material's Representative Volume Element with a very fine mesh, i.e. a huge amount of CPU time with classical methods used for simulations such as the Finite Element Method.

Numerical approaches based on the FFT for calculating the stress and strain fields within a composite material received a surge of interest since the pioneering work of Moulinec and Suquet [23,24]. They were first developed to compute effective properties and mechanical field of linear elastic composites[23–26] and were extended to heterogeneous materials with eigenstrains (dislocations, thermal strains…) [14,27–30]. They are also used for conductivity problems [31] , non-linear materials [25,27], viscoplastic or elastoviscoplastic polycrystals [32–36]. Today, FFT based approaches represent alternative to finite element method because they are rather attractive in terms of computation time [32].

However initial tests indicate that the displacement field computed (essential for diffraction pattern generation) with FFT algorithms presents some numerical artifacts. These numerical artifacts are due to Gibbs phenomenon or ''aliasing'' and to voxelization. The accuracy of the calculated strain or displacement field is strongly influenced by these shortcomings and the simulated peaks may provide wrong information on mechanical behavior or material characteristics. Therefore, it is important to control these artifacts to simulate correct diffraction pattern in the case of a microstructure containing different phases, grains, and crystal defects.

The aim of this paper is to improve the accuracy of the displacement field for diffraction peak generation. This improvement is based on the introduction of a consistent discrete periodized Green operator associated with the displacement field in order to take explicitly into account the discreteness of the discrete Fourier Transform method [37]. The improvement of the voxelization in FFT-method is performed through a sub-voxelization method will be described for inclined dislocation loops. These improvements are reported and discussed. In the section 2, the FFT-based method to compute the displacement field in a periodic medium is described. In section 3, the treatment of voxelization problems in FFT-based approaches by a sub-voxelization method is detailed in the case of slip plane not conforming to FFT grid. In the section 4, simulation of diffraction peaks is reported and discussed.

2. Displacement field

2.1. FFT-based algorithm and mechanical fields

Let us consider a homogeneous elastic medium with eigenstrain assuming a periodic unit cell discretized in $N \times N \times N$ voxels and subjected to an uniform overall strain tensor denoted $\boldsymbol{E}$. Here, this overall strain is the spatial average of the strain field in the unit cell (with external loading and a

given eigenstrain field). The unit cell contains dislocations (line defects) which are modeled with an eigenstrain tensor. These dislocations create a displacement field during their motion along various slip systems and thus generates strain/stress field [38].

The displacement vector is denoted $\boldsymbol{u}$ and in the forthcoming equations, $\boldsymbol{x}$ denotes any position vector within the unit cell. All vectorial and tensorial fields will be written using bold characters.

Starting from the equation for mechanical equilibrium, $div\,\boldsymbol{\sigma}(\boldsymbol{x}) = 0$, and using elastic equations, the displacement field is given at every positions by [39]:

$$\boldsymbol{u}(\boldsymbol{x}) = (\boldsymbol{B} * \boldsymbol{c^0}\!:\boldsymbol{\varepsilon}^*)(\boldsymbol{x}) \quad (1)$$

Where the symbol $*$ denotes the spatial convolution product, $\boldsymbol{c^0}$ is the homogeneous linear elastic stiffness, $\boldsymbol{\varepsilon}^*$ is the eigenstrain field and $\boldsymbol{B}$ is a third order Green operator defined in Fourier space as:

$$\widehat{B_{ijk}}(\boldsymbol{\xi}) = \frac{i}{2}\left(\widehat{G_{ij}}\xi_k + \widehat{G_{ik}}\xi_j\right) \quad (2)$$

in which $\widehat{\boldsymbol{B}}$ is the Fourier transform of $\boldsymbol{B}$ and $\widehat{\boldsymbol{G}}$ is the Fourier transform of the elastic Green tensor [39]. Therefore, using the Fourier transform of spatial convolution product, Equation (1) can be written in Fourier space as:

$$\hat{\mathbf{u}}(\boldsymbol{\xi}) = \widehat{\mathbf{B}}(\boldsymbol{\xi})\!:\mathbf{c^0}\!:\widehat{\boldsymbol{\varepsilon}^*}(\boldsymbol{\xi}) \quad (3)$$

Several numerical results showed that the use of the third order operator $\widehat{\boldsymbol{B}}$ derived from the classic Green $\widehat{\boldsymbol{G}}$ leads to spurious oscillations on the computed displacement field near materials discontinuities. The Discrete Fourier transform (DFT) used in this algorithm indeed transforms a periodic function in real space into a periodic function in reciprocal space. However, the operator $\widehat{\boldsymbol{B}}$ commonly used is the continuous analytic operator truncated to the size of the unit cell of the reciprocal space: it is not periodic function. To fix this problem, we a periodized consistent discrete Green operator using the DFT. The Fourier transform of this new operator $\widehat{\boldsymbol{B'}}$ is written as function of $\widehat{\boldsymbol{B}}$ (the mathematical details about its derivation are given in [37]) and reads:

$$\widehat{\boldsymbol{B}}'(\xi_{ijk}) = A_{ijk}\sum_{m,n,p=-\infty}^{+\infty}\frac{(-1)^{m+n+p}}{(mN+i)}\frac{1}{(nN+j)}\frac{1}{(pN+k)}\widehat{\boldsymbol{B}}(\xi_{mN+i,nN+j,pN+k})$$

$$\text{With}\qquad A_{ijk} = \left(\frac{N}{\pi}\right)^3 sin\left(\frac{i\pi}{N}\right)sin\left(\frac{j\pi}{N}\right)sin\left(\frac{k\pi}{N}\right) \quad (4)$$

Discrete frequency appearing in this equation is given when N is even by (T is the unit cell period):

$$\boldsymbol{\xi} = \left(-\frac{N}{2}+1\right)\frac{1}{T},\left(-\frac{N}{2}+2\right)\frac{1}{T},\ldots,-\frac{1}{T},0,\frac{1}{T},\ldots.\left(\frac{N}{2}-1\right)\frac{1}{T},\left(\frac{N}{2}\right)\frac{1}{T}$$

Here the sum on the $\widehat{\boldsymbol{B}}$ operator is extended to the whole reciprocal space (in practice for m, n, p up to a few tens) and folded up onto the unit cell of the DFT with suitable coefficients. The inverse transform of $\hat{\boldsymbol{u}}(\boldsymbol{\xi})$ gives the displacement field at the center of each voxel.

We can also compute the displacement field at each voxel's corner with a shifted operator using the shift theorem:

$$\widehat{\boldsymbol{B}}''(\xi_{ijk}) = A_{ijk}e^{p\pi\frac{\boldsymbol{i+j+k}}{N}}\sum_{m,n,p=-\infty}^{+\infty}\frac{1}{(mN+i)}\frac{1}{(nN+j)}\frac{1}{(pN+k)}\widehat{\boldsymbol{B}}(\xi_{mN+i,nN+j,pN+k}) \quad (5)$$

2.2. Numerical examples

Let us consider a homogeneous material with isotropic elastic constant: Young's modulus $E = 333.4\,GPa$ and the Poisson ration $\vartheta = 0.26$. This approximately corresponds to the room temperature elastic constants of single crystalline Ni-based Superalloys. The unit cell (Figure 1a) is discretized in $128 \times 128 \times 128$ voxels and contains a square-shaped inclusion discretized in

$32 \times 32 \times 1$ voxels corresponding to an Eshelby-like square prismatic loop perpendicular to the z-axis. In order to generate a shift of the upper surface of the inclusion relative to its lower surface by a Burgers vector $\boldsymbol{b}(0, 0, b_3)$ the voxels within the inclusion are submitted to an eigenstrain: $\boldsymbol{\varepsilon}^*_{ij} = 0$ except $\boldsymbol{\varepsilon}^*_{33} = 1$. We thus have $b_3 = t \times \boldsymbol{\varepsilon}^*_{33}$ where t the thickness of the inclusion in the z-direction (i.e. the voxel size). This displacement field computed with the FFT algorithm using the different periodized discrete Green operators is represented along z-axis in figure 1.

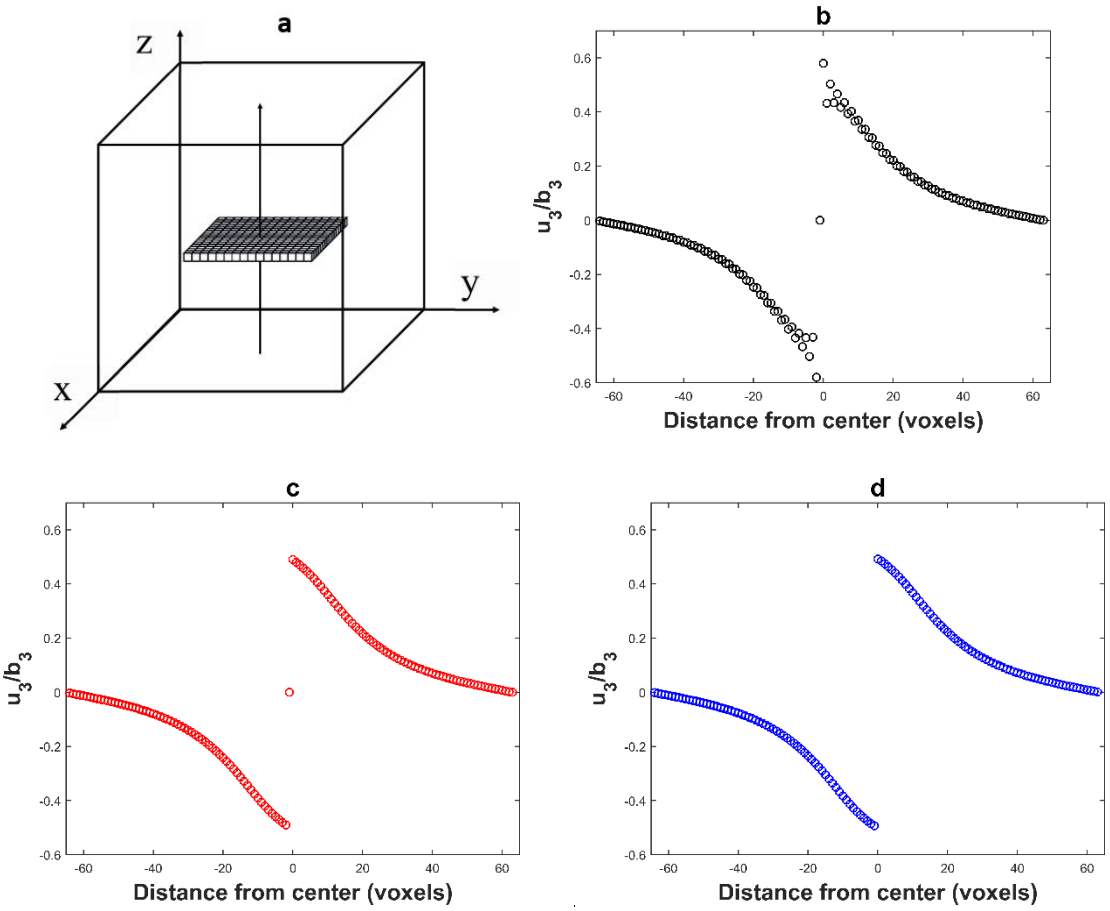

Figure 1: (a) Simulation of a squared dislocation in plane (001) by a platelet with eigenstrain; (b) Component u_3 of the displacement field (normalized by b_3) along the z axis (arrow) computed with the Green operator $\boldsymbol{B}$ and showing oscillations; (c) Same component correct u_3 computed with $\boldsymbol{B}'$ The displacement at voxel (64,64,64) is zero in the center of the inclusion (c) and $b_3/2$ on its surface (c). (d) Same component correct u_3 computed with $\boldsymbol{B}''$.

When computed along a line crossing a dislocation loop, the displacement field exhibits a discontinuity with a jump equal to Burgers vector $\boldsymbol{b}$. This is indeed observed in figure 1. However, the displacement field computed with the usual Green operator $\boldsymbol{B}$ (figure 1b) also shows oscillations, while which are not observed with the periodized operators $\boldsymbol{B}'$ and $\boldsymbol{B}''$. An artificial damping of the oscillations in figure 1b (such as a low pass filtering) might smooth these oscillations, but it would also smooth the discontinuity.

2.3. Voxelization effect on the displacement field.

While the displacement field computed for dislocation loops having their planes parallel to the faces of the simulated volume, artifacts appear for inclined loops, as shown in figure 2 for a dislocation loop with a $[0\bar{1}1]$ Burgers vector lying in a (111) slip plane of a fcc crystal. The eigenstrain tensor is constrained in the region occupied by the dislocation loop (transformed voxels) and is given by:

$$\varepsilon_{ij}^{*} = \frac{A_s}{2V}\left(n_i b_j + n_j b_i\right) \quad (6)$$

where A_s is the area on which planes with normal $\boldsymbol{n}(n_1, n_2, n_3)$ has slipped by a relative amount $\boldsymbol{b}(b_1, b_2, b_3)$ and V is the volume occupied by the loop [40,41]. As before, the dislocation loop is 32 voxels wide in the x and y directions, and 1 voxel thick but now with a z position such that $x + y + z = constant$. The displacement has been computed at the center of voxels with the periodized operator $\boldsymbol{B}'$ along z (figure 2b). As in figure 1c, the displacement in the center of a voxel belonging to the loop plane (black dot in the reddish transformed voxel in figure 2b) is zero. The displacement in the first neighboring voxels (red dot in figure 2b) are shifted relative to the expected position, so that the displacement difference between these voxels is significantly lower than **b,** see figure 2c. It can be checked in figure 2b that each of these voxels shares three faces with a transformed voxel. A more detailed analysis shows that the second neighbors (which share three edges with transformed voxels) are also slightly shifted in the opposite direction. The result is shown in figure 2d with: a strong localized oscillation of the phase (taken here as the displacement modulo **b).**

Although the amplitude of this shift is small (less than 10% of the Burgers vector) it has unwanted consequences on the diffraction peak simulation:

- The dislocation loops are surrounded by four impaired layers of voxels: As the scattered X-Ray amplitude is proportional to the Fourier transform of **G·u** (see equation (8) in section 4) we can expect a phantom streak in the intensity in a direction perpendicular to the loop plane.
- The displacement field near the edges of the loop (near the dislocation line) will be quite different from its expected value, and the strain field will not vary with the distance r to the dislocation line as $1/r$. This will strongly affect the tails of the diffraction peaks

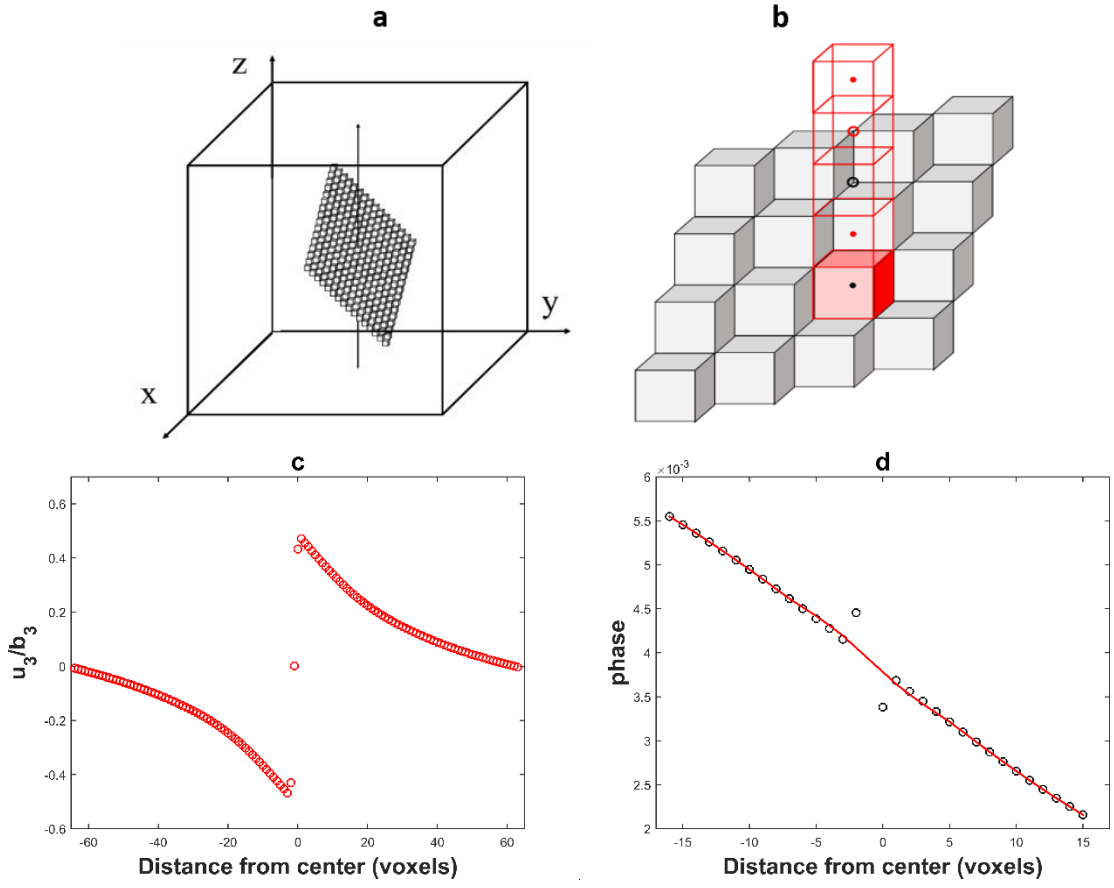

Figure 2. (a) Modeling of a squared dislocation loop in a (111) plane as a layer of voxels with eigenstrain; (b) position of the computed points relative to the transformed voxels with eigenstrains; (c) Plot of the displacement field u_3 (normalized by b_3) along the z direction for dislocation loop

illustrated on figure 2. (d) Local oscillation of the phase due to the voxelization of the dislocation loop (the representation is made for 32 voxels centered in the unit cell along z direction). The red line is approximately equal to the phase expected for this displacement field.

3. Sub-voxelization method to correct voxelization effects.

3.1. Sub-voxelization method

The (conceptually) simplest way to remove this voxelization artifact would be to work on a multiple grid (to multiply the number of voxels along each direction by 2, 4, or more), then to downsample the displacement field data. In that case, FFT algorithms would lose much of their interest due to these more demanding computational efforts. We show below that this can be done in a more economical way by applying a patch to the FFT-computed displacement field. The basic method is to compute *on the same grid* the difference vector:

$$\Delta_i(\boldsymbol{x}) = u_i^{sub}(\boldsymbol{x}) - u_i^{hom}(\boldsymbol{x}) \quad (7)$$

where $u_i^{sub}(\boldsymbol{x})$ is the displacement vector calculated for voxels where this eigenstrain is concentrated on a single plane of sub voxels (figure 3b) and u_i^{hom} the displacement field in direction i of voxels with a uniform eigenstrain (figure 3a). For the sake of clarity, we use 2D diagrams in Figure 3, but here the technique is applied to real 3D problems.

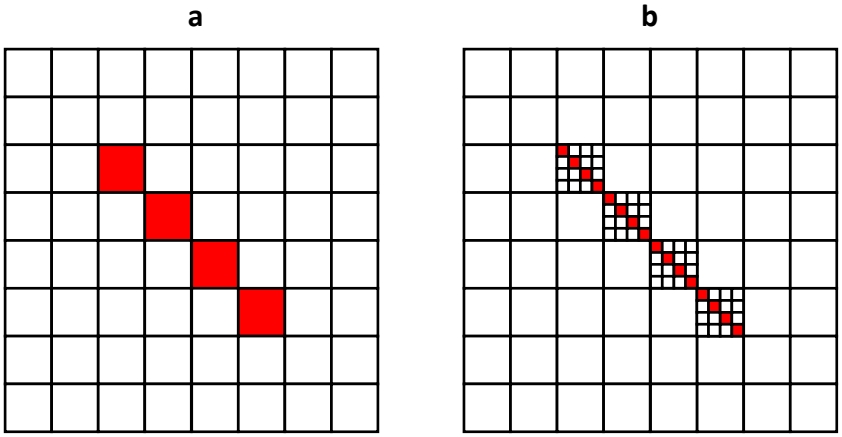

Figure 3. 2D representation of a dislocation loop in a tilted plane on a (8 × 8) FFT grid. (a) With a homogeneous eigenstrain in the voxels occupied by the dislocation loop. (b) With each voxel subdivided into 4*4 sub-voxels, only 4 of which are eigenstrained.

In order to compute the displacement due to sub-voxels, we use a $N \times N$ ($N \times N \times N$) grid for 2D (resp. 3D) problems where each voxel can be subdivided into $n \times n$ ($n \times n \times n$) sub voxels. Only n ($n \times n$) sub voxels are submitted to an eigenstrain field. At a point $\boldsymbol{A}$ of the grid (black dots, figure 4a), we need to compute the sum of the displacements $\boldsymbol{u_i^j}$ due to the n ($n \times n$) sub voxels j (center $\boldsymbol{B_j}$) within a voxel centered at point $\boldsymbol{O}$. This sum is equivalent to the sum of the displacements due to a strained sub voxel at point $\boldsymbol{O}$ on the grid points $\boldsymbol{A_j}$ such as $\boldsymbol{OA_j = B_jA}$ (figure 4b). It is also equivalent to the sum of the displacements $\boldsymbol{u'^j_i}$ due to a *full* voxel at point $\boldsymbol{O}$ on the initial grid on points $\boldsymbol{A'_j}$ such as $\boldsymbol{OA'_j} = n\boldsymbol{B_jA}$ (figure 4c). The only difference between these last two sums is due to the long-range strain field, and approximately results in a linear drift of the displacement. As the end of the vectors $\boldsymbol{OA'_j}$ does not lie on the grid points (voxel centers) but on the corners of the voxels, the $\boldsymbol{u'^j_i}$ displacements must be calculated with the shifted operator $\boldsymbol{B''}$ (equation (5)). A last point is the scaling of the $\boldsymbol{u_i^j}$ and $\boldsymbol{u'^j_i}$ sums during the operations of figure 4. To keep the one Burgers vector jump between both sides of the sub voxels plane in Figure 4a, the eigenstrain in the sub voxels must be multiplied by n. The backwards change of scale requires a division by n: there is no scaling factor between u_i^{hom} and $u_i^{sub} = \sum u'^j_i$.

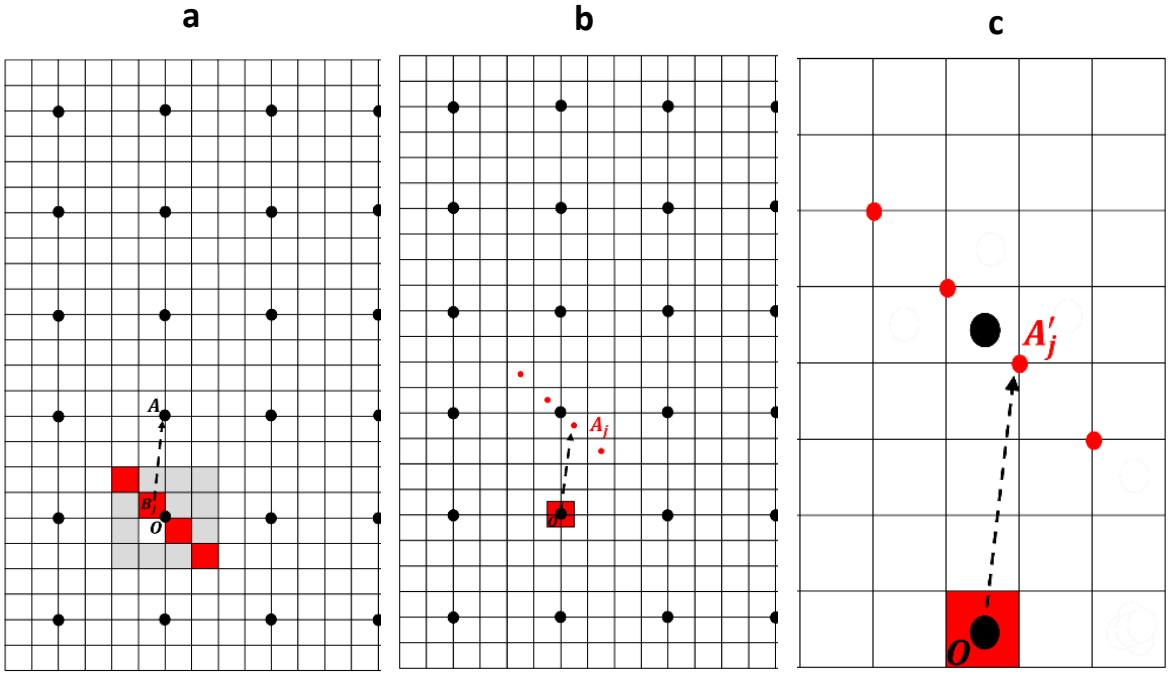

Figure 4. (a). 2D representation of the computational grid. Black dots correspond to the voxels center. A voxel with center O is discretized in 4×4 in 2D ($4 \times 4 \times 4$ in 3D) sub-voxels. Some sub-voxels contain an eigenstrain (red sub-voxels). We want to compute the displacement field at voxel centered at point A, due to these deformed sub-voxels centered at B_j. (b) Effect of one deformed sub-voxel centered at O on a row of sub-voxels centered at B_j such as $\boldsymbol{OA_j = B_jA}$. The sum of these effects is equal to the previous displacement field. (c) Effect of deformed voxels centered at O on a row of voxels (computed at corners $\boldsymbol{A'_j}$ using Green operator $\boldsymbol{B''}$) such as $\boldsymbol{OA'_j = nB_jA}$. This sum is equal to previous wanted sum.

We need to compute $\Delta_{ij\_pl}(\boldsymbol{x})$ the difference in displacement in direction i due to a voxel which belongs to the plane "pl" (for fcc ''pl'' is equal to $(111), (\bar{1}11), (1\bar{1}1), (11\bar{1})$) of a dislocation loop with a Burgers vector j at a position x relative to the transformed voxel. In practice, in a material with cubic symmetry, it is sufficient to compute $\Delta_{13\_(111)}(\boldsymbol{x})$ and $\Delta_{33\_(111)}(\boldsymbol{x})$, and to use the symmetries of the cube (fourfold [001] axis, threefold [111] axis, and $(1\bar{1}0)$ symmetry plane) (and suitable exchanges of the components of $\boldsymbol{x}$) to obtain the required components. As it can be seen in figure 2b, $\Delta_{ij\_pl}(\boldsymbol{x})$ is non-zero only for the neighbors of the transformed voxel, except the drift due to the long range strain alluded above. The final recipe to compute $\Delta_{ij\_pl}(\boldsymbol{x})$ and use the patch becomes:

- Compute the field $\boldsymbol{c^0 : \varepsilon^*}$ defined in equation (1) for an isolated voxel with the eigenstrain associated to a dislocation loop (equation (6)) with a Burgers vector [001] in a (111) plane (see figure 2).
- Compute the displacement field in directions x($\boldsymbol{u_1^{hom}}$) and z ($\boldsymbol{u_3^{hom}}$) at the voxels' center around the transformed voxel by convolution with the discrete periodized operator $\boldsymbol{B'}$ (equation (4))
- Compute the displacement field in directions x and z at the voxels' corners around the transformed voxel by convolution with the shifted operator $\boldsymbol{B''}$ (equation (5))
- Calculate the $\boldsymbol{u_1^{sub}} = \sum \boldsymbol{u'^j_1}$ **and** $\boldsymbol{u_3^{sub}} = \sum \boldsymbol{u'^j_3}$ sums ($n \times n$ terms for each sum) as in figure 4c, then the raw $\Delta_{13(111)}(\boldsymbol{x})$ and $\Delta_{33\_(111)}(\boldsymbol{x})$ for (x_1, x_2, x_3) going from -3 to 3 times the voxel size t.
- Use the farthest voxels to correct the drift of the components so that all terms for large $\boldsymbol{x}$ are zero, and keep only the terms for the first three neighbors non zero. .

The patch can then be applied on the raw (FFT-based) displacement field by adding the convolution of all transformed voxels of the different slip systems by the relevant $\Delta_{ij\_pl}(\boldsymbol{x})$.

3.2. Results

For tests, we used the same $128 \times 128 \times 128$ grid as above, and the transformed voxel was divided into 8*8*8 sub voxels (using a reference medium with the same elastic constants as before). Only the final values in units of b (after drift correction) of $\Delta_{13\_(111)}(\boldsymbol{x})$ and $\Delta_{33\_(111)}(\boldsymbol{x})$ are used and others components are obtain by symmetries (Appendix A).

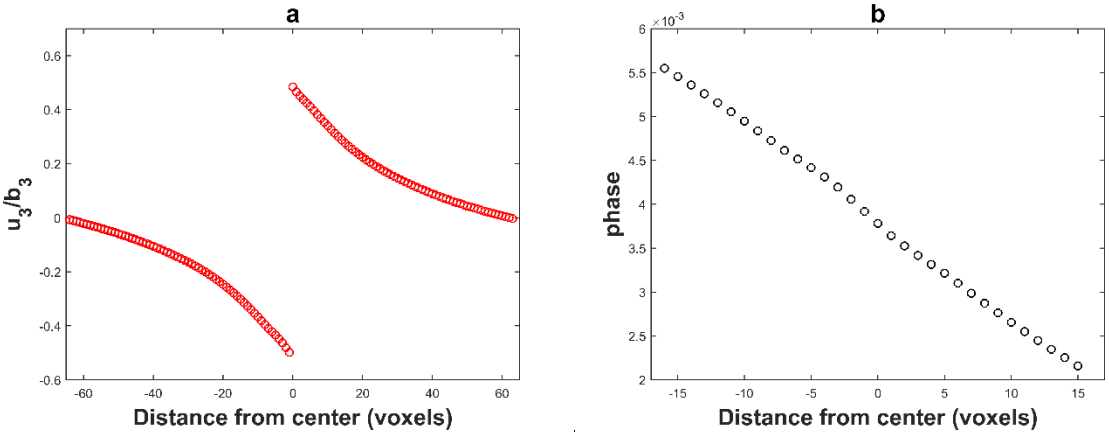

Figure 5. (a) Plot of the displacement field u_3 (normalized by b_3) along the z direction for dislocation loop illustrated on figure2. Artifacts are removed by sub-voxel method described above. (b) the phase (i.e. the displacement modulo a Burgers vector). With this correction, the phase is almost continuous.

The patch was used on the same configuration as in figure2. Figure 5a shows the resulting displacement field and figure 5b the phase (i.e. the displacement modulo a Burgers vector) in Burgers vector units. As it can be observed from figure 5a, the artifacts of the displacement field have disappeared. In addition, the resulting phase varies smoothly even during the crossing of the dislocation loop, see figure 5b.

4. Application on diffraction peak simulation

In this section, we show simulated diffraction peaks in order to point the effects of voxelization artifacts and of the patch on numerical results. Under kinematical conditions and assuming a coherent beam, the amplitude of a diffracted wave at a position $\boldsymbol{q}$ in the vicinity of a reciprocal $\boldsymbol{G}$ lattice vector is [14,18,42–44]:

$$A(\boldsymbol{q}) = FT[A_0(\boldsymbol{r}) \times F(\boldsymbol{G}, \boldsymbol{x}) \times exp(-2i\pi\, \boldsymbol{G} \cdot \boldsymbol{u}(\boldsymbol{x}))] \quad (8)$$

where $\boldsymbol{x}$ is the position of the scattering atom, $A_0(\boldsymbol{x})$ is the amplitude of the incidence wave, $F(\boldsymbol{G}, \boldsymbol{x})$ is the local structure factor and $\boldsymbol{u}(\boldsymbol{x})$ the displacement field. The scattered intensity is $I(\boldsymbol{q})= |A(\boldsymbol{q})|^2$. For a face-centered cubic crystal, this intensity is non zero when **G** (h, k, l) is such as h, k, and l have the same parity. Here two diffraction vectors **G** (200) and **G** (002) are used. They respectively correspond to **G**·**b** = 0 and **G**·**b** = 1. The 3D diffracted intensity has been calculated using the FFT instead of the continuous Fourier Transform, then summed in the planes perpendicular to the **G** vector to obtain a linear plot along **G** equivalent to a I(2θ) plot. In figures 6a (**G** (200)) and 6c (**G**(002)), we show the diffracted intensity (logarithmic scale) as a function of the pixel position i, and in figures 6b and 6d a logarithmic/logarithmic plot of the intensity vs. $|i - i_0|$ where i_0 is the center of the peak. In order to only study the effect of the displacement fields, we set $\mathrm{A}_0(\boldsymbol{x}) = 1$ and $\mathrm{F}(\mathbf{G}, \boldsymbol{x}) = 1$ for these simulations.

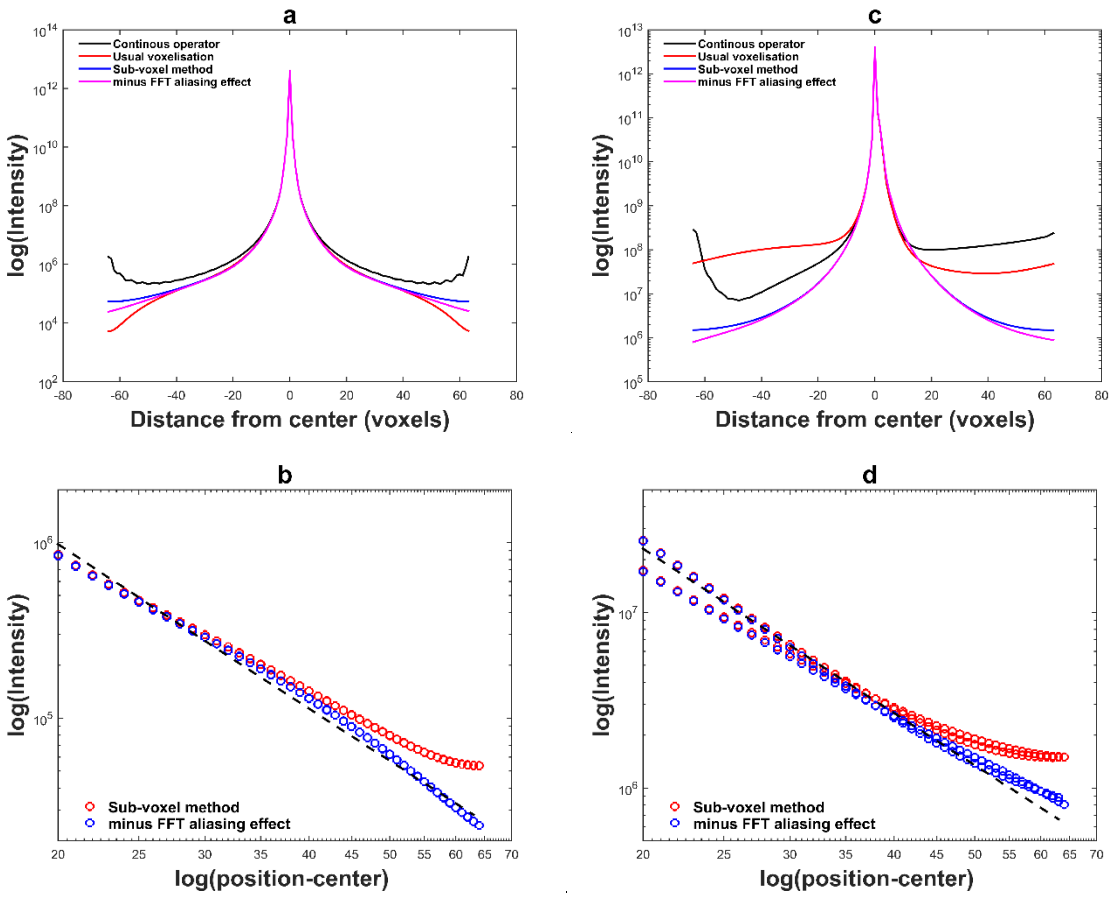

Figure 6. Simulated diffracted intensity as a function of the pixel position (logarithmic scale) . 3D configuration is represented in 1D plot by making sum in each plane along an x-axis. Different way for computing the displacement fields are studied for a dislocation loop with a $[0\bar{1}1]$ Burgers vector lying in a (111) slip plane . (a) Diffracted vector studied is **G** (200) corresponding to **G**·**b** = 0. (b) log/log representation of the intensity vs. $|i - i_0|$. (c) and (d) Same as (a) et (b) but the studied diffracted vector is **G** (002).

The peak shape near the top of the peaks is the same for both computing methods. It is perfectly symmetric in the **G**·**b** = 0 case and exhibits a bump on the right side for **G**·**b** = 1. Their long-range behavior is however quite different. When the displacement field has been calculated with the usual truncated operator (black line), a phantom peak is observed at large $|i - i_0|$ (at large q), which is due to the short period oscillations near the displacement field discontinuity (Figure 1a). The behavior of the peak calculated with the modified Green operator (blue curve) is only slightly better: the intensity at large q is underestimated in one case and overestimated in the other. When the intensity has been calculated with the sub voxel patch (red curve) the long range intensity follows the expected $I_0|i - i_0|^{-3}$ law [45,46]: the peak tails are indeed related to the highly distorted zones near the dislocations' cores. However, the red curve saturates at very large **q**. We suppose this is due to the use of the Fast Fourier Transform instead of the continuous Fourier Transform in the calculation of the scattered amplitude (equation (8)): The plot of figure 6 represents only one period in Fourier space, and is repeated over and over on all Fourier space. We can now calculate the intensity of the tails of these repetitions:

$$I_{neib.} = \sum I_0|i - i_0 - 128m|^{-3} \quad (9)$$

where m varies from -5 to 5 (zero excluded). We obtain the pink curve at the bottom of figures 5a and 5c. If we now plot the difference between the red intensity curve and this pink background line, we obtain the green curve. On the log./log. plots, figure 6b and 6d it can be checked that this curve follows the $I_0|i - i_0|^{-3}$ law to the end. Thus, the residual error in the intensity computed by FFT results of the FFT itself, and not from a residual error on the sub voxel corrected displacement field. If the

number of voxels is increased to 512^3 or 1024^3 while keeping the physical size of the Representative Volume constant this residual error should fall down to undetectable levels.

5. Conclusions

In this paper, we showed that although the use of a periodized Green operator in the FFT-based method improves the final displacement field solution in a Representative Volume containing discontinuities (dislocation loops), artifacts due to the voxelization of the dislocation loop planes are still present with respect to analytical solutions. These artifacts have unwanted consequences on the tails of diffraction peaks simulated by using this displacement field as input data.

We have introduced a patch which corrects these artifacts by simulating the displacement field which would be obtained with a much finer voxelization without need to do the computations on a finer grid. A simple construction method for this patch has been given and the patch can be used in a single post-processing step to modify the initial FFT-based displacement field.

The modified displacement field has been used to simulate one-dimensional diffraction peaks. The procedure strongly improves the shape of the peaks' tails, i.e. it gives a good description of the displacement field near the dislocation lines.

Acknowledgments: This work was supported by the French State through the program "Investment in the future" operated by the National Research Agency (ANR) and referenced by ANR-11-LABX-0008-01 (LabEx DAMAS). Gabor Ribarik greatly acknowledge the support of the Janos Bolyai Research Fellowship of the Hungarian Academy of Sciences.

Author Contributions: For the present paper, Komlavi S. Eloh performed the simulation work and wrote the first draft of the paper; Alain Jacques analyzed numerical results and helped the simulation part; Gabor Ribarik helped in constructing the computer code and helped in analyzing results; Stéphane Berbenni helped in developing the first theoretical part of the paper. The paper was written by Komlavi S. Eloh, Alain Jacques and Stéphane Berbenni.

Conflicts of Interest: The authors declare no conflict of interest.

Appendix A

$\Delta_{\mathbf{33\_(111)}}(\boldsymbol{x_1, x_2, x_3})$ **and** $\Delta_{\mathbf{13\_(111)}}(\boldsymbol{x_1, x_2, x_3})$ have these symmetries due to the permutation properties of the plan $(\mathbf{111})$

$$\Delta_{33\_(111)}(x_1, x_2, x_3) = \Delta_{33\_(111)}(x_2, x_1, x_3)$$
$$\Delta_{33\_(111)}(x_1, x_2, x_3) = -\Delta_{33\_(111)}(-x_1, -x_2, -x_3)$$
$$\Delta_{13\_(111)}(x_1, x_2, x_3) = -\Delta_{13\_(111)}(-x_1, -x_2, -x_3)$$

The others values of $\Delta_{ij\_(111)}(\boldsymbol{x})$ are given as function of $\Delta_{33\_(111)}(x_1, x_2, x_3)$ and $\Delta_{13\_(111)}(x_1, x_2, x_3)$**:**

$\Delta_{11\_(111)}(x_1, x_2, x_3) = \Delta_{33\_(111)}(x_3, x_2, x_1)$ $\quad$ $\Delta_{12\_(111)}(x_1, x_2, x_3) = \Delta_{13\_(111)}(x_1, x_3, x_3)$

$\Delta_{22\_(111)}(x_1, x_2, x_3) = \Delta_{33\_(111)}(x_1, x_3, x_2)$ $\quad$ $\Delta_{31\_(111)}(x_1, x_2, x_3) = \Delta_{13\_(111)}(x_3, x_2, x_1)$

$\Delta_{32\_(111)}(x_1, x_2, x_3) = \Delta_{13\_(111)}(x_3, x_1, x_2)$ $\quad$ $\Delta_{21\_(111)}(x_1, x_2, x_3) = \Delta_{13\_(111)}(x_1, x_3, x_2)$

$\Delta_{23\_(111)}(x_1, x_2, x_3) = \Delta_{13\_(111)}(x_2, x_1, x_3)$

The value of $\Delta_{33}(x_1, x_2, x_3)$ and $\Delta_{13}(x_1, x_2, x_3)$ for the remaining plane $(\bar{1}11), (1\bar{1}1), (11\bar{1})$ are obtained using these symmetries:

$\Delta_{33\_(\bar{1}11)}(x_1, x_2, x_3) = \Delta_{33\_(111)}(x_2, -x_1, x_3)$ $\quad$ $\Delta_{13\_(\bar{1}11)}(x_1, x_2, x_3) = \Delta_{13\_(111)}(-x_1, x_2, x_3)$

$\Delta_{33\_(1\bar{1}1)}(x_1, x_2, x_3) = \Delta_{33\_(111)}(-x_2, x_1, x_3)$ $\quad$ $\Delta_{13\_(1\bar{1}1)}(x_1, x_2, x_3) = \Delta_{13\_(111)}(x_1, -x_2, x_3)$

$\Delta_{33\_(11\bar{1})}(x_1, x_2, x_3) = -\Delta_{33\_(111)}(x_2, x_1, -x_3)$ $\quad$ $\Delta_{13\_(11\bar{1})}(x_1, x_2, x_3) = -\Delta_{13\_(111)}(x_1, x_2, -x_3)$

References

1. Graverend, J.-B. L.; Dirand, L.; Jacques, A.; Cormier, J.; Ferry, O.; Schenk, T.; Gallerneau, F.; Kruch, S.; Mendez, J. In Situ Measurement of the γ/γ′ Lattice Mismatch Evolution of a Nickel-Based Single-Crystal

Superalloy During Non-isothermal Very High-Temperature Creep Experiments. *Metall and Mat Trans A* **2012**, *43*, 3946–3951, doi:10.1007/s11661-012-1343-x.
2. Robinson, I.; Harder, R. Coherent X-ray diffraction imaging of strain at the nanoscale. *Nat Mater* **2009**, *8*, 291–298, doi:10.1038/nmat2400.
3. Pfeifer, M. A.; Williams, G. J.; Vartanyants, I. A.; Harder, R.; Robinson, I. K. Three-dimensional mapping of a deformation field inside a nanocrystal. *Nature* **2006**, *442*, 63.
4. Ungár, T. Strain Broadening Caused by Dislocations Available online: https://www.scientific.net/MSF.278-281.151 (accessed on Jun 16, 2018).
5. Ungár, T.; Gubicza, J.; Ribárik, G.; Borbély, A. Crystallite size distribution and dislocation structure determined by diffraction profile analysis: principles and practical application to cubic and hexagonal crystals. *Journal of applied crystallography* **2001**, *34*, 298–310.
6. Ribárik, G.; Ungár, T.; Gubicza, J. MWP-fit: a program for multiple whole-profile fitting of diffraction peak profiles by ab initio theoretical functions. *Journal of Applied Crystallography* **2001**, *34*, 669–676.
7. Ribárik, G.; Gubicza, J.; Ungár, T. Correlation between strength and microstructure of ball-milled Al–Mg alloys determined by X-ray diffraction. *Materials science and engineering: A* **2004**, *387*, 343–347.
8. Balogh, L.; Ribárik, G.; Ungár, T. Stacking faults and twin boundaries in fcc crystals determined by x-ray diffraction profile analysis. *Journal of applied physics* **2006**, *100*, 023512.
9. Groma, I. X-ray line broadening due to an inhomogeneous dislocation distribution. *Physical Review B* **1998**, *57*, 7535.
10. Tréhorel, R.; Ribarik, G.; Schenk, T.; Jacques, A. Real time study of transients during high temperature creep of a Ni-based superlloy by far field high energy synchrotron X-rays diffraction. *Journal of applied crystallography(under review)*.
11. Tréhorel, R. Comportement mécanique haute température du superalliage monocristallin AM1: Etude in-situ par une nouvelle technique de diffraction en rayonnement synchrotron, Université de Lorraine: Nancy, France, 2018.
12. Bernier, J. V.; Park, J.-S.; Pilchak, A. L.; Glavicic, M. G.; Miller, M. P. Measuring Stress Distributions in Ti-6Al-4V Using Synchrotron X-Ray Diffraction. *Metallurgical and Materials Transactions A* **2008**, *39*, 3120–3133, doi:10.1007/s11661-008-9639-6.
13. Miller, M. P.; Bernier, J. V.; Park, J.-S.; Kazimirov, A. Experimental measurement of lattice strain pole figures using synchrotron x rays. *Review of Scientific Instruments* **2005**, *76*, 113903, doi:10.1063/1.2130668.
14. Jacques, A. From Modeling of Plasticity in Single-Crystal Superalloys to High-Resolution X-rays Three-Crystal Diffractometer Peaks Simulation. *Metallurgical and Materials Transactions A* **2016**, *47*, 5783–5797, doi:10.1007/s11661-016-3793-z.
15. Weisbrook, C. M.; Gopalaratnam, V. S.; Krawitz, A. D. Use of finite element modeling to interpret diffraction peak broadening from elastic strain distributions. *Materials Science and Engineering: A* **1995**, *201*, 134–142, doi:10.1016/0921-5093(95)09757-0.
16. Miller, M. P.; Dawson, P. R. Understanding local deformation in metallic polycrystals using high energy X-rays and finite elements. *Current Opinion in Solid State & Materials Science* **2014**, *5*, 286–299, doi:10.1016/j.cossms.2014.09.001.
17. Demir, E.; Park, J.-S.; Miller, M. P.; Dawson, P. R. A computational framework for evaluating residual stress distributions from diffraction-based lattice strain data. *Computer Methods in Applied Mechanics and Engineering* **2013**, *265*, 120–135, doi:10.1016/j.cma.2013.06.002.
18. Vaxelaire, N.; Proudhon, H.; Labat, S.; Kirchlechner, C.; Keckes, J.; Jacques, V.; Ravy, S.; Forest, S.; Thomas, O. Methodology for studying strain inhomogeneities in polycrystalline thin films during in situ thermal loading using coherent x-ray diffraction. *New J. Phys.* **2010**, *12*, 035018, doi:10.1088/1367-2630/12/3/035018.
19. Song, X.; Xie, M.; Hofmann, F.; Illston, T.; Connolley, T.; Reinhard, C.; Atwood, R. C.; Connor, L.; Drakopoulos, M.; Frampton, L. Residual stresses and microstructure in powder bed direct laser deposition (PB DLD) samples. *International Journal of Material Forming* **2015**, *8*, 245–254.
20. Hofmann, F.; Song, X.; Jun, T.-S.; Abbey, B.; Peel, M.; Daniels, J.; Honkimäki, V.; Korsunsky, A. M. High energy transmission micro-beam Laue synchrotron X-ray diffraction. *Materials Letters* **2010**, *64*, 1302–1305.
21. Hofmann, F.; Abbey, B.; Liu, W.; Xu, R.; Usher, B. F.; Balaur, E.; Liu, Y. X-ray micro-beam characterization of lattice rotations and distortions due to an individual dislocation. *Nature communications* **2013**, *4*, 2774.

22. Suter, R. M.; Hennessy, D.; Xiao, C.; Lienert, U. Forward modeling method for microstructure reconstruction using x-ray diffraction microscopy: Single-crystal verification. *Review of Scientific Instruments* **2006**, *77*, 123905, doi:10.1063/1.2400017.
23. Moulinec, H.; Suquet, P. A numerical method for computing the overall response of nonlinear composites with complex microstructure. *Computer Methods in Applied Mechanics and Engineering* **1998**, *157*, 69–94, doi:10.1016/S0045-7825(97)00218-1.
24. Moulinec, H.; Suquet, P. Fast numerical method for computing the linear and nonlinear properties of composites. *Comptes Rendus de l'Académie des Sciences. Série II* **1994**, *318*.
25. Michel, J. C.; Moulinec, H.; Suquet, P. A computational scheme for linear and non-linear composites with arbitrary phase contrast. *International Journal for Numerical Methods in Engineering* **2001**, *52*, 139–160.
26. Müller, W. Mathematical vs. Experimental Stress Analysis of Inhomogeneities in Solids. *Journal de Physique IV Colloque* **1996**, *06*, C1-139-C1-148, doi:10.1051/jp4:1996114.
27. Vinogradov, V.; Milton, G. W. An accelerated FFT algorithm for thermoelastic and non-linear composites. *International Journal for Numerical Methods in Engineering* **2008**, *76*, 1678–1695, doi:10.1002/nme.2375.
28. Anglin, B. S.; Lebensohn, R. A.; Rollett, A. D. Validation of a numerical method based on Fast Fourier Transforms for heterogeneous thermoelastic materials by comparison with analytical solutions. *Computational Materials Science* 2014, 209–217.
29. Graham, J. T.; Rollett, A. D.; LeSar, R. Fast Fourier transform discrete dislocation dynamics. *Modelling Simul. Mater. Sci. Eng.* **2016**, *24*, 085005, doi:10.1088/0965-0393/24/8/085005.
30. Berbenni, S.; Taupin, V.; Djaka, K. S.; Fressengeas, C. A numerical spectral approach for solving elasto-static field dislocation and g-disclination mechanics. *International Journal of Solids and Structures* **2014**, *51*, 4157–4175, doi:10.1016/j.ijsolstr.2014.08.009.
31. Eyre, D. J.; Milton, G. W. A fast numerical scheme for computing the response of composites using grid refinement. *Eur. Phys. J. AP* **1999**, *6*, 41–47, doi:10.1051/epjap:1999150.
32. Prakash, A.; Lebensohn, R. A. Simulation of micromechanical behavior of polycrystals: finite elements versus fast Fourier transforms. *Modelling Simul. Mater. Sci. Eng.* **2009**, *17*, 064010, doi:10.1088/0965-0393/17/6/064010.
33. A. Lebensohn, R. N-site modeling of a 3D viscoplastic polycrystal using Fast Fourier Transform. *Acta Materialia* **2001**, *49*, 2723–2737, doi:10.1016/S1359-6454(01)00172-0.
34. Lebensohn, R. A.; Rollett, A. D.; Suquet, P. Fast fourier transform-based modeling for the determination of micromechanical fields in polycrystals. *JOM* **2011**, *63*, 13–18, doi:10.1007/s11837-011-0037-y.
35. Lebensohn, R. A.; Kanjarla, A. K.; Eisenlohr, P. An elasto-viscoplastic formulation based on fast Fourier transforms for the prediction of micromechanical fields in polycrystalline materials. *International Journal of Plasticity* **2012**, *32–33*, 59–69, doi:10.1016/j.ijplas.2011.12.005.
36. Suquet, P.; Moulinec, H.; Castelnau, O.; Montagnat, M.; Lahellec, N.; Grennerat, F.; Duval, P.; Brenner, R. Multi-scale modeling of the mechanical behavior of polycrystalline ice under transient creep. *Procedia IUTAM* **2012**, *3*, 76–90, doi:10.1016/j.piutam.2012.03.006.
37. Eloh, K. S.; Jacques, A.; Berbenni, S. Development of a new consistent discrete Green operator for FFT-based methods to solve heterogeneous problems with eigenstrain. *International Journal of Plasticity(submitted)* 2018.
38. Hirth, J. P.; Lothe, J. *Theory of Dislocations*; Krieger Publishing Company, 1982; ISBN 978-0-89464-617-1.
39. Mura, T. *Micromechanics of Defects in Solids*; Mechanics of Elastic and Inelastic Solids; 2nd ed.; Springer Netherlands, 1987; ISBN 978-90-247-3256-2.
40. Li, Q.; Anderson, P. M. A Compact Solution for the Stress Field from a Cuboidal Region with a Uniform Transformation Strain. *Journal of Elasticity* **2001**, *64*, 237–245, doi:10.1023/A:1015203721914.
41. Anderson, P. M. Crystal-based plasticity. *Fundamentals of Metals Forming* 1982, 277–279.
42. Takagi, S. A Dynamical Theory of Diffraction for a Distorted Crystal. *Journal of the Physical Society of Japan* **1969**, *26*, 1239–1253, doi:10.1143/JPSJ.26.1239.
43. Vartanyants, I. A.; Yefanov, O. M. Coherent X-ray Diffraction Imaging of Nanostructures. *arXiv:1304.5335 [cond-mat]* **2013**.
44. Takagi, S. Dynamical theory of diffraction applicable to crystals with any kind of small distortion. *Acta Crystallographica 15*, 1311–1312, doi:10.1107/S0365110X62003473.
45. Ungár, T. Microstructural parameters from X-ray diffraction peak broadening. *Scripta Materialia* **2004**, *51*, 777–781, doi:10.1016/j.scriptamat.2004.05.007.

460 46. Krivoglaz, M. A. Theory of X-Ray and Thermal Neutron Scattering by Real Crystals; Springer US, 1969;
461 ISBN 978-1-4899-5584-5.